

Intergalactic-Absorption Confounding Circumgalactic Observations

ITAI BROMBERG,¹ KARTICK C. SARKAR,^{2,3} ORLY GNAT,¹ AND YUVAL BIRNBOIM¹

¹*Centre for Astrophysics and Planetary Science, Racah Institute of Physics, The Hebrew University, Jerusalem 91904, Israel*

²*Dept of Astrophysics, Tel Aviv University, Tel Aviv, Israel*

³*Dept of Space, Planetary & Astronomical Sciences and Engineering, Indian Institute of Technology Kanpur, Kanpur, India*

ABSTRACT

The origin of warm ions in the circum-galactic medium (CGM) surrounding massive galaxies remains a mystery. In this paper, we argue that a significant fraction of the observed warm-ion columns may arise in the intergalactic medium (IGM) surrounding galactic halos. We use a simple spherical collapse model of the dark matter (DM) halos and their baryonic content to compute the evolving ion fractions within and outside virial halos. We show that the photoionized IGM may produce a thick blanket of warm ions around the CGM, thereby contaminating CGM observations. We find that the IGM contributes $> 75\%$ of the total O VI column densities in halos with virial masses exceeding a few times $10^{11} M_{\odot}$, and that it may dominate the O VI absorption even for lower mass-halos, depending on the impact parameter. We compare our results with observations and find that our simplified model reproduces the overall O VI columns as well as their trend with the impact parameter and halo mass. We show that observed warm ion columns may be completely dominated by the IGM envelopes, consistent with CGM² data. We, therefore, suggest that theoretical interpretations of CGM-survey observations must consider the possible contribution of the surrounding IGM. Although our simplified model suggests that it may be possible to kinematically distinguish between CGM and IGM origins through the absorption line profiles, this distinction is likely unfeasible in realistic astrophysical halos, due to the complex velocity structure in the multi-phased CGM.

Keywords: galaxies: general, halos, intergalactic medium – ultraviolet: galaxies

1. INTRODUCTION

The circum-galactic medium (CGM) plays an essential role in galaxy formation and evolution, by controlling gas inflow into galaxies and outflow from them. While various aspects of the complex, multi-phased, CGM have been extensively studied, the roles that different physical processes play in determining its internal structure and ionization properties remain unclear and are the focus of intense observational and theoretical work (Prochaska et al. 2011b; Tumlinson et al. 2011; Shen et al. 2012; Muzahid et al. 2012; Werk et al. 2013; Lehner et al. 2014; Werk et al. 2016; Oppenheimer et al. 2016; Stern et al. 2016; Gutcke et al. 2017; Suresh et al. 2017; Tumlinson et al. 2017; Faerman et al. 2017, 2020). The cosmological theory of galaxy formation indicates that galactic halos form as gas from the diffuse intergalactic medium (IGM) falls onto the dense regions where

galaxies form. While dark matter (DM) particles oscillate about the center of the potential well, baryons are shock-heated to a “virial temperature”, corresponding to the mass of the forming galaxy. These shock-heated halos are natural sites for the production of highly ionized species. However, warm ions may also be produced outside the virial radius, in the surrounding intergalactic medium. In this region, the baryonic density and temperature profiles are still affected by the halo’s gravity, as well as by radiation fields (shock-self radiation, UV background, etc), strong outflows, cosmic rays, and the inhomogeneity of the cosmic web.

Observational campaigns such as the *COS*-Halos survey (Tumlinson et al. 2011), IMACS survey (Johnson et al. 2015), or CGM² survey (Tchernyshyov et al. 2022) have examined the extent of warm ions (e.g. C IV, O VI) surrounding galaxies, as revealed via absorption features in the spectra of background-quasars. These studies focus on $\gtrsim L_{\star}$ galaxies ($10^{11.5} \lesssim M_{\text{halo}} \lesssim 10^{13} M_{\odot}$) at various impact parameters ($10 \lesssim b \lesssim 400$ kpc) and relatively low redshifts ($0.1 \lesssim z \lesssim 0.6$). The *COS*-Halos survey (Tumlinson et al. 2011) demonstrates the existence of O VI absorption, at

impact parameters up to 150 kpc, with no apparent trend of the column density with impact-parameter within this range. Later, [Johnson et al. \(2015\)](#) used a larger data sample (*COS-Halos+IMACS*), and showed that no O VI absorption is detected at impact parameters above the virial radius, with upper-limits $\sim 10^{13.4} \text{ cm}^{-2}$. Their findings suggest that O VI resides primarily within the halo¹. [Tchernyshyov et al. \(2022\)](#) used the CGM² data sample to study the extent of O VI absorption. They found that O VI is detected out to their maximal surveyed impact parameter, of ~ 400 kpc, without any particular trend, and with upper limits of order 10^{14} cm^{-2} . According to their fit, significant O VI columns may persist up to $(2 - 3)R_{200}$, depending on the halo mass. For lower mass ($\gtrsim 0.1L_*$) galaxies, [Prochaska et al. \(2011b\)](#) used the LCO/WFCCD survey ([Prochaska et al. 2011a](#)) to explore a much larger range of impact parameters, extending out to ~ 1000 kpc. They found a large covering fraction of O VI outside the galactic halos, particularly for sub- L_* galaxies. They associated it with the diffuse medium surrounding individual galaxies. The prevalence of O VI in and around galactic halos thus remains inconclusive.

Detailed 3D cosmological simulations of galaxy formation attempt to reproduce key trends in observational surveys, by invoking various physical processes and assumptions (e.g. radiative cooling, ionization, star formation and evolution, chemical enrichment, wind feedback, black hole growth, AGN feedback, cosmic dust, etc.). [Nelson et al. \(2018\)](#) used the IllustrisTNG simulations, to estimate the O VI abundance around galaxies. They found that O VI columns persist out to an impact parameter of 10 Mpc, due to contributions by nearby satellite halos and the IGM (Figure 9 therein). They showed that although the halo’s contribution to the O VI column density drops at roughly the virial radius, there are significant contributions from other sources outside the central halo, that prevent a distinct cut-off in the column density.

[Oppenheimer et al. \(2018\)](#) used the EAGLE zoom-in simulations, to probe O VI columns at impact parameters below ~ 300 kpc. Their results indicate a slow decline in the O VI column with impact parameter, regardless of halo mass (see Figure 2 therein). In a later paper by [Ho et al. \(2021\)](#), an EAGLE simulation also produced a flat O VI column density vs. impact parameter profile, with contributions from gas outside $3R_{\text{vir}}$. [Appleby et al. \(2022\)](#) used SIMBA to study different ion absorption features and their origin. They estimated that O VI absorption is comprised of roughly equal contributions from the gas inside and outside the halo (their Figure 7, and analysis therein).

An alternative to cosmological hydrodynamic simulations is the use of semi-analytic 1D models, which aim to explain the observed trends by focusing on key physical processes. Several works have focused on identifying the origin of O VI, and the ionization mechanisms which dominated its production. [Stern et al. \(2018\)](#) considered the possibility that O VI is produced either in the shocked halo or in a low-pressure photo-ionized layer outside the accretion shock. Their low-pressure scenario requires that the accretion shock be located well within R_{vir} . This low-pressure O VI phase is disfavored by cosmological simulations but can reproduce the observed properties of O VI as well as other absorption features.

[McQuinn & Werk \(2018\)](#) and [Qu & Bregman \(2018\)](#) explored the dominant ionization mechanism for O VI production in the CGM. [McQuinn & Werk \(2018\)](#) included radiative cooling and feedback and showed that inside the halo, O VI is probably produced collisionally, with large cooling gas flows regulated by feedback. [Qu & Bregman \(2018\)](#) considered a similar model but also took into account photoionization and steady-state cooling, and demonstrated that photoionization may play a key role in lower mass halos, as well as in the outskirts of massive halos, due to the lower densities.

[Voit \(2019\)](#) introduced precipitation-regulated feedback models, which account for the relatively constant O VI column density over large spans of halo masses and impact parameters. The emphasis on precipitation has been inspired by the velocity profiles of detected O VI, which do not exceed the halos’ escape velocity. This suggests that the gas is circulated inside the halo. Furthermore, this supports the notion that the CGM is multiphased, consistent with the simultaneous detection of various ionic species.

In [Faerman et al. \(2017\)](#), a 1D multiphased semi-analytic model based on isothermal hydrostatic profiles has been presented. Assuming turbulent-driven log-normal distributions for the densities and temperatures of both the warm ($\sim 10^4\text{K}$) and hot phases, the model reproduced the detections and upper limits from [Tumlinson et al. \(2011\)](#) and [Johnson et al. \(2015\)](#). [Faerman et al. \(2020\)](#) extended the multiphased model to isentropic profiles, and allowed for radius-dependent temperatures and non-thermal contributions. Their profiles for the hot gas were calibrated using data from [Tumlinson et al. \(2011\)](#) and [Johnson et al. \(2015\)](#). As these models extend only slightly beyond R_{vir} , they predict a decline in column density at larger radii.

While warm-ions column densities serve as common diagnostics for CGM analysis and interpretation, theoretical models do not usually account for the warm ions produced outside the shock radius, where the halo’s presence still affects the baryon-density profile. Computationally, even though simulation-based studies may naturally include this component, they do not focus on the role that the IGM plays in absorption line observations. This is particularly true for low

¹ However, they state that upper limits of $N_{\text{OVI}} > 10^{14} \text{ cm}^{-2}$ are not shown, due to constraints sensitivity considerations. See [Johnson et al. \(2015\)](#) for details

mass galaxies ($M_{\text{vir}} \lesssim 10^{11} M_{\odot}$) where the observations show a significant presence of O VI in contrast to the theoretical CGM models that fail to predict such behavior. This further motivates us to study the IGM contribution to the warm ions at different mass scales. As we will see, in our model the origin of O VI around low-mass galaxies is mainly from the surrounding IGM and not the CGM.

In this work, we argue that the gravitational focusing around halos, which is a natural and unavoidable consequence of structure formation in Λ CDM cosmology, creates a favorable site for warm-ion production (including O VI) via photoionization by the ambient background radiation. We demonstrate this notion using a highly simplified 1D toy model. We show that significant amounts of O VI should naturally arise outside R_{shock} , thus increasing – and sometimes dominating – the observed columns of O VI and other key ions around galaxies.

In §2 we describe our simplified 1D model. This includes the evolving properties of the dark matter halos and the distribution and ionization properties of the baryonic matter both within and outside galactic halos. In §3 we discuss the observational signatures that arise in our simplified halos. We compute the expected absorption line columns and discuss the relative contributions of the shocked gas within the halo versus photoionized gas in the IGM to the total absorption-line signatures. We discuss the possibility of discerning them observationally based on their kinematic properties. We conclude in §4.

2. MODEL DESCRIPTION

We use a simple 1D cosmological toy model to study the impact of the halos’ gravitational potentials and the UV background on the warm-ions production in halos and their surrounding IGM. The model consists of three major components - i) A redshift-dependent dark matter density profile, ii) Evolving baryonic density and velocity profiles, and iii) The corresponding temperature and ionization states of the baryonic matter. We describe these model ingredients below.

2.1. Spherical Collapse Model

A simplified model for the dark matter halo profiles is constructed by tracing the evolution of initial overdensity perturbations solely under the influence of gravity, in an Einstein-de-Sitter (EdS) cosmology. We follow the numerical procedures used in Birnboim & Dekel (2003) to set the initial conditions for each 1D spherical simulation. Our profiles are constructed from shells, each tracing a cycloid of the form,

$$r = A(1 - \cos \eta) \quad (1)$$

$$t = B(\eta - \sin \eta) \quad (2)$$

(e.g. Ryden 2017), where η is the conformal time.

We determine each shell’s free parameters (A and B) by imposing two requirements: one at an early linear stage, and the other at the epoch of virialization. First, we require that the mass enclosed within r at some early linear stage ($\eta \ll 1$), satisfies that the overdensity at that time, $\delta(M) \equiv \bar{\rho}/\rho_u - 1$ is proportional to the correlation function of the power spectrum of the universe (Dekel 1981). In this expression, $\bar{\rho}$ is the average density inside r , and ρ_u is the universal density. The proportionality constant between $\delta(M)$ and the correlation function can be determined by requiring that a specific mass virializes at a specific time after the Big Bang, within our EdS framework. For each shell, we fix B by requiring that at the time of the shell’s perspective virialization (when $\eta = 3\pi/2$), the radius r and the time t will satisfy $r = r_{\text{vir}}$ and $t = r_{\text{vir}}/v_{\text{vir}}$, with $v_{\text{vir}}^2 = GM/r_{\text{vir}}$ with M the mass enclosed within that shell. This ensures that the infall velocity at this stage is v_{vir} .

Here, we calculate profiles with collapsed masses (at $z = 0$) between $10^{11} - 10^{14} M_{\odot}$. We solve eqns. 1 and 2 for 1000 shells with the outermost shells exceeding the virial and turnaround radii. The dark matter density at a given radius is calculated numerically by differentiating the mass with respect to the radii of two adjacent shells at each time (for more details see Birnboim & Dekel 2003), and the results are then mapped onto a regular $r - t$ grid extending to 10 Mpc.

2.2. Gaseous Halo

Given the evolving dark matter profiles, we compute the properties of the baryonic matter both within and outside the shock radius, defined as:

$$R_{\text{shock}} = f_{\text{shock}} R_{\text{vir}}, \quad (3)$$

where f_{shock} is a dimensionless multiplication factor. We explore different values of f_{shock} (0.5, 1, 1.5, and 2) to account for uncertainties in the extent of the virialized gas. The virial radii of halos with present-day DM masses of $10^{11}, 10^{12}, 10^{13}, 10^{14} M_{\odot}$, at redshift $z = 0.2$, are $R_{\text{vir}} \approx 80, 170, 365, 790$ kpc, respectively.

We set the gas density to be everywhere proportional to the evolving dark matter density,

$$\rho_{\text{gas}}(r) = f_b \rho_{\text{dm}}(r), \quad (4)$$

with $f_b = 0.165$, the universal baryonic fraction (Shull et al. 2012; Planck Collaboration et al. 2016) (c.f. $f_b = 0.13$ in Birnboim & Dekel 2003).

For the velocities, we follow Birnboim & Dekel (2003) and set

$$v = v_{\text{vir}} \frac{\sin \eta}{1 - \cos \eta} \quad (5)$$

outside R_{shock} . Inside the halo, we set $v_{\text{CGM}} = 0$.

2.3. Metallicity

For the baryonic component, we assume a metallicity,

$$Z = \begin{cases} 0.03 Z_{\odot}, & r \geq R_{\text{shock}} \\ 0.1 Z_{\odot}, & r < R_{\text{shock}}, \end{cases}$$

inspired by CGM (e.g. [Lehner et al. 2019](#)) and IGM (e.g. [Dalton et al. 2021, 2022](#), $Z = 0.02 - 0.05 Z_{\odot}$) observations.

Determining the metallicity in and around halos is an active area of research (e.g. [Wiersma et al. 2011](#); [Gatuzz et al. 2024](#); [Strawn et al. 2024](#)), with a broad range of possible values. Consequently, the absorption line column densities may need to be adjusted once a "typical" metallicity is established. In the CGM, the metal-ion columns are generally proportional to the metallicity. The IGM columns are slightly more sensitive to metallicity due to the impact it may have on the thermal properties of the gas (see below).

2.4. Temperature and Ionization State

When determining the thermal and ionization properties of the gas, we assume that the gas is everywhere (both within and outside the halo) exposed to the [Haardt & Madau \(2012\)](#) redshift-dependent metagalactic UV background radiation field. Given the radiation field, we use CLOUDY-v17.01 ([Ferland et al. 2017](#); [Chatzikos et al. 2023](#)), to obtain the thermal equilibrium temperatures, and ion fractions as described below.

We assume that the gas within R_{shock} has a uniform metallicity, $Z = 0.1 Z_{\odot}$, and a temperature T_{CGM} such that

$$T_{\text{CGM}} = \max(T_{\text{PIE}}, T_{\text{vir}}). \quad (6)$$

In this expression, T_{vir} is the virial (collisional shock) temperature, which depends on the halo's mass and the redshift. We follow [Johnson \(2012\)](#) (eq. 1 therein) and set,

$$T_{\text{vir}} = 4 \times 10^4 \left(\frac{\mu}{1.2} \right) \left(\frac{M_{\text{vir}}}{10^8 h^{-1} M_{\odot}} \right)^{2/3} \left(\frac{1+z}{10} \right) \text{K}, \quad (7)$$

where $h \approx 0.7$ is the dimensionless Hubble constant μ is the mean molecular weight (≈ 0.6 for a fully ionized gas).

T_{PIE} is the thermal equilibrium temperature which, given the redshift-dependent background radiation, is a function of the local density, $\rho_{\text{gas}}(r)$.

For the ionization of the CGM gas, we take into account the combined impact of collisional ionization at the (forced) halo temperature T_{CGM} (eqn. 6), and photoionization by the ambient background. We refer to this ionization state as the collisional photo-ionization equilibrium (CPIE).

For the IGM, the ionization and thermal states of the gas are computed assuming a thermal- and ionization equilibrium in the presence of a metagalactic UV background.

2.5. Column Densities

Given the run of ion fractions with radius, we can now compute the column densities as functions of the impact parameter. The column density of element m with ionization level i is given by:

$$N_i^m = \int n_i^m(s) ds = 2 \int_b^{r_{\text{max}}} \frac{n^m(r) x_i^m(r)}{\sqrt{1 - \left(\frac{b}{r}\right)^2}} dr \quad (8)$$

where we integrate along a line-of-sight intersecting the halo at an impact parameter b . $n_i^m(s)$ is the number density of element m in ionization state i . In the second integral, x_i^m is the ion fraction of element m at ionization level i , $n^m = n_{\text{H}} A^m Z$ is the number density of element m , n_{H} is the total Hydrogen number density, A^m is the solar elemental abundance, and Z is the metallicity. The factor of 2 is a geometrical factor that accounts for the two sides of the spherical halo.

Since we focus on the ions produced outside the galactic disk, we do not integrate over radii smaller than $0.1 R_{\text{vir}}$. The interstellar medium within the galactic disk would highly contaminate any detection at lower impact parameters.

When estimating the IGM contribution to the total absorption line signatures, we set the maximal integration radius, $r_{\text{max}} = 3 \text{ Mpc}$. In our model, this outer radius corresponds to an expansion velocity offset of approximately $\Delta v \simeq 200 \text{ km/s}$ for halos with masses in the range² of $\sim 10^{11} - 10^{12} M_{\odot}$ at $z \simeq 0.2$.

2.6. Absorption Lines Kinematics

Given the density, temperature, and velocity distribution in our halos, we compute the kinematic line profiles, at a given impact parameter. In doing so, we assume that the line-profile within each shell is well approximated by a Gaussian profile at the appropriate temperature, centered about the shells' velocity, and we accumulate the optical depth per frequency through the different shells. The numerical procedure is briefly described in appendix A.

To validate this kinematic approximation, we also use the TRIDENT Python package ([Hummels et al. 2017](#)). TRIDENT computes absorption line profiles given the density, temperature, and velocity profiles. This module is set to simulate an observation with the *Cosmic Origins Spectrograph* on board the *Hubble Space Telescope*, using a G130M line-spread function kernel. TRIDENT also introduces the Milky Way foreground and a Gaussian noise to the simulated line, for a more direct comparison with observations.

² However, for more massive halos, the included velocity range beyond the turnaround radius decreases, whereas for group-sized objects $\gtrsim 5 \times 10^{13} M_{\odot}$, this radius remains within the collapsing region.

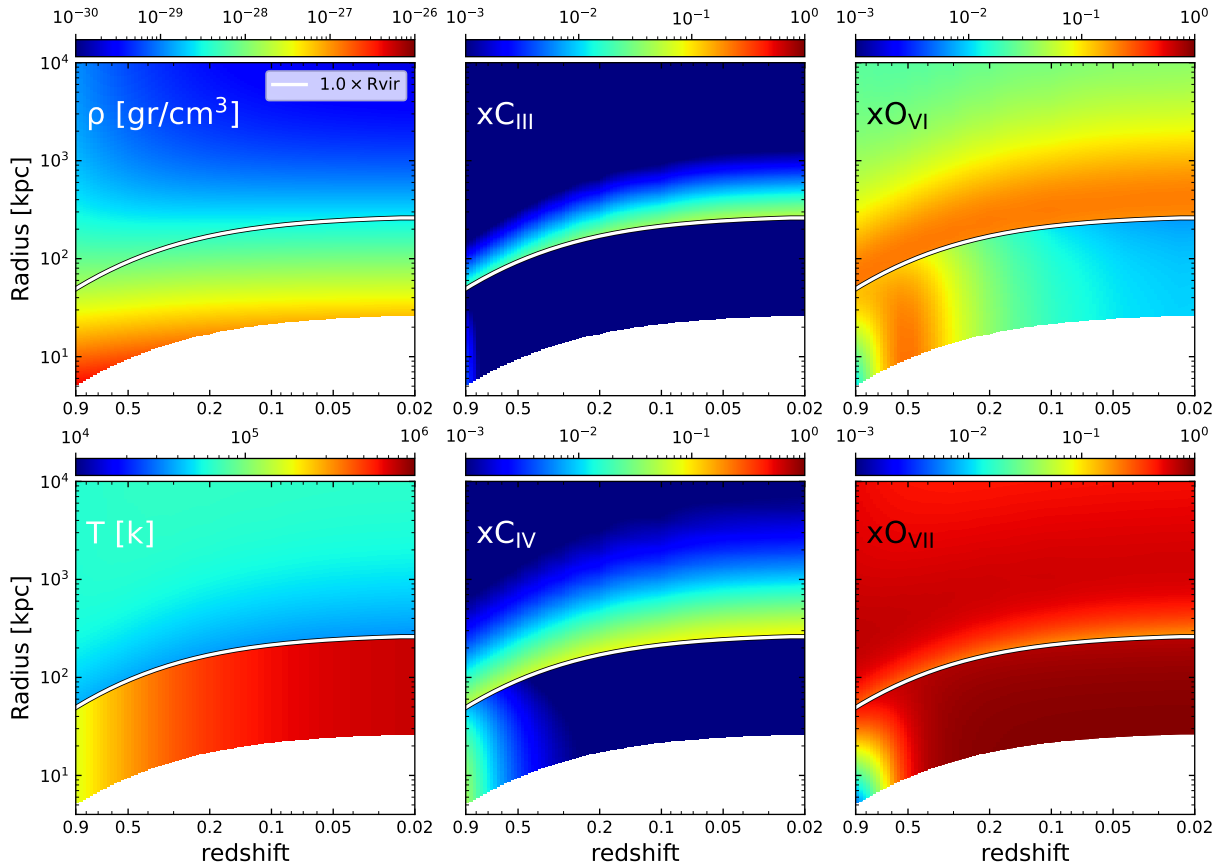


Figure 1. Radius-redshift diagrams, for a $M_{z=0} = 10^{12} M_{\odot}$ halo, color-coded by different quantities. Top-left: baryonic gas density; bottom-left: gas temperature, top middle: C III ion fraction, bottom-middle: C IV ion fraction, top-right: O VI ion fraction, bottom-right: O VII ion fraction. The white curve in each panel shows the shock radius vs. redshift, with $f_{\text{shock}} = 1$. We do not consider radii below $0.1R_{\text{vir}}$.

We performed these calculations, including all the shells between $\max(0.1R_{\text{vir}}, b) - 3$ Mpc for the total observed columns, and again for the IGM – this time including only shells that are outside the halo, between $\max(R_{\text{shock}}, b) - 3$ Mpc.

2.7. Limitations

Our constructed CGM model is highly simplified and does not accurately capture many details of astrophysical halos: It does not account for the morphological, thermal, and dynamical complexities of the multi-phased CGM or the radiative and dynamical properties of the accretion shocks. Nevertheless, as we will demonstrate in the following sections, it approximately reproduces the observed column densities, both within and beyond R_{vir} . Our primary objective in this paper is to assess the contribution of the IGM to the warm-ion absorption, and we consider this simplified model to be adequate for this specific purpose.

3. RESULTS

3.1. Ion fractions

Figure 1 shows the evolution of our fiducial halo model, for a halo that attains a mass of $10^{12} M_{\odot}$ at redshift $z = 0$, with $f_{\text{shock}} = 1$ ($R_{\text{shock}} \approx 260$ kpc at $z = 0$). The evolution of various quantities is shown using color maps on the redshift-radius plane. The bottom-left panel shows the evolution of the gas temperature. The gas temperature is determined either by equilibrium with the UV background radiation at the local density, or by the shock temperature for virialized gas – if it is larger than the equilibrium temperature – following equation 6. The baryonic gas density is shown in the top-left panel and follows from equation 4.

We display the evolving ion fraction distributions for C III, C IV, O VI, and O VII in the middle and right columns of Figure 1. The ion fractions at C PIE are functions of temperature, density, and redshift. Note, that while the density profile $\rho(r)$ varies slowly with redshift, the virial temperature and the intensity of the UV -background radiation are stronger functions of z . Consequently, the ion fractions at a given density are also redshift-dependent.

Figure 1 confirms that far from the halo, the density approaches its undisturbed mean value, resulting in an equilibrium temperature of $T_{\text{PIE}} \sim 5 \times 10^4$ K. Warm ions are

produced in this dilute warm gas due to photoionization. As the IGM gas falls toward the halo, the gas density (ρ_{gas}) rises while the equilibrium temperature (T_{PIE}) drops, enhancing the production of warm ions such as C III, C IV, etc. The figure shows that significant fractions of warm ions are produced outside the virial radius, even at low redshifts. Specifically, O VI is efficiently produced in the low-density IGM down to $z = 0$. We also see that ions such as O VI can extend nearly a Mpc beyond the CGM forming a widespread envelope of ions around the halo.

Inside the CGM ($r < R_{\text{shock}}$), collisional ionization at the virial temperature is generally the dominant ionization process. As the halo evolves, it becomes more massive, and the CGM temperature increases from $\approx 10^5$ K at $z \sim 1$ to $\approx 10^6$ K at $z \approx 0$. Accordingly, the O VI ion fraction in CGM increases as the halo evolves, peaking at $z \sim 0.5$ before decreasing again. At $z \lesssim 0.5$, the CGM becomes hot enough to support the production of higher ions like O VII.

3.2. Column densities

To test the detectability of the IGM component, we now compute the column densities at various impact parameters. As mentioned above, we define the CGM column as that arising from $r = 0.1R_{\text{vir}}$ to R_{shock} , and the IGM column as that arising from $r = R_{\text{shock}}$ to 3 Mpc. The total column density is the sum of the two.

In the top panel of Figure 2, we show the total (solid) and IGM-only (dashed) O VI column densities, for the same halo shown in Figure 1, at redshift, $z = 0.2$ (when its mass is $10^{11.6} M_{\odot}$). The different colors display results for different values of f_{shock} , vs. impact parameter. The gray markers show detections from the CGM² survey, as presented in Tchernyshyov *et al.* (2022). The top panel in figure 2 demonstrates that, regardless of the choice of f_{shock} , our highly simplified model produces O VI column densities comparable to observations. It also demonstrates that the IGM columns are comparable to both the total column densities and the observations. We thus argue that the near-halo IGM may significantly contribute to observed warm-ion column densities in CGM surveys.

The bottom panel of figure 2 compares our results for the case of $f_{\text{shock}} = 1$ (black curves, identical to orange curves in the upper panel), with the median column densities computed by Nelson *et al.* (2018) from *IllustrisTNG* simulations (colored curves). In addition to the total column densities, Nelson *et al.* (2018) also provide an “other” component, emanating from IGM gas and satellite halos. As in the top panel, solid lines correspond to the total columns and dashed lines are for gas outside the halo. Each color is for a different halo mass (see labels). Note, that Nelson *et al.* (2018) provide columns for $z = 0$ halos, while our curve is for a $z = 0.2$ halo, to allow for a more direct comparison with observa-

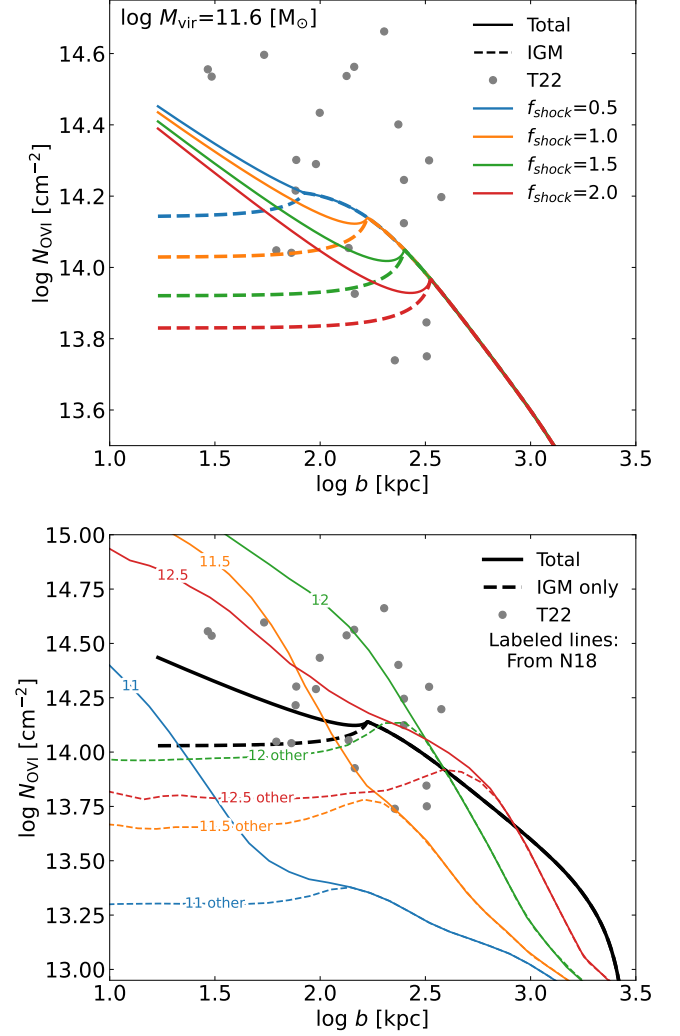


Figure 2. Top panel: O VI column densities vs. impact parameter, for the same halo shown in Figure 1, at $z = 0.2$ when $M_{\text{vir}}(z = 0.2) = 10^{11.6} M_{\odot}$. The solid curves show the total column density (from $\max(0.1R_{\text{vir}}, b)$ to 3 Mpc). The dashed curves show the IGM contribution (from $\max(R_{\text{shock}}, b)$ to 3 Mpc). Different colors are for different values of f_{shock} . Bottom panel: A comparison of our model (black curve) for $f_{\text{shock}} = 1$ with the median O VI column densities from Nelson *et al.* (2018) for various halo masses (see labels) at $z = 0$. Solid curves are for total column densities, and dashed curves are for the gas beyond the shock radius. In both panels, the gray markers show detections from Tchernyshyov *et al.* (2022).

tions. Although our model yields a more gradual slope overall, our IGM component is comparable to the $10^{11.5-12.5} M_{\odot}$ halos “other” curves by Nelson *et al.* (2018). The broad agreement of our computed columns with both observations and complex 3D-simulations serves as a sanity check when using our simplified model to estimate IGM contributions to O VI column densities.

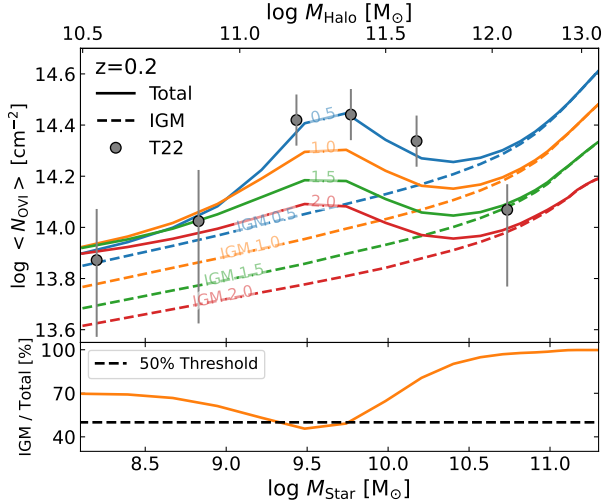


Figure 3. Top: Surface-averaged values of O VI column densities (see text) vs stellar-mass. The solid curves show the total column densities and the dashed curves show the IGM column densities. Different colors are for different values of f_{shock} (see labels). The gray markers display the CGM² results from [Tchernyshyov et al. \(2022\)](#). Bottom: fraction (percent) of the IGM-O VI column from the total O VI column densities, for $f_{\text{shock}} = 1$. The dashed horizontal line marks a 50% IGM contribution to the total estimated columns.

To explore how the overall IGM contribution fractions depend on halo mass, and to compare our results with other works, we now consider surface-averaged columns – representing the entire halo – as was previously done in [Nelson et al. \(2018\)](#) and [Tchernyshyov et al. \(2022\)](#).

To determine the surface averages, we first calculate the total- and IGM-columns³ as functions of the impact parameter, b . Subsequently, we surface-average these columns over impact parameters ranging from $b = 0.1R_{\text{vir}}$ to $b = R_{\text{shock}}$ enabling a direct comparison with published results.

The top panel of figure 3 shows the surface-averaged total (solid) and IGM-only (dashed) O VI column densities vs. the halo’s stellar mass M_{Star} . The corresponding halo masses are shown on the top axis. The stellar masses were obtained using the stellar-to-halo mass relation presented in [Girelli et al. \(2020\)](#) (equation 6 and table 1 therein). Different colors are for different values of f_{shock} . The gray markers display the CGM² detections from [Tchernyshyov et al. \(2022\)](#). We find a good agreement between the observations and our model’s total column densities, for $f_{\text{shock}} = 1$, even when the CGM dominates. We note that our highly simplified model exhibits a trend similar to the *IllustrisTNG* results presented in [Nelson et al. \(2018\)](#), albeit shifted by approximately half a decade in mass (see Figure 6 in [Tchernyshyov et al. \(2022\)](#)). Our

model aligns more closely with observational data, whereas the *IllustrisTNG* results tend to favor higher masses by about a factor of 3.

The nice agreement of our model with the CGM² data at the lower mass range ($M_{\text{vir}} \lesssim 10^{11} M_{\odot}$) is particularly important: Low-mass galaxies are not expected to host stable CGMs due to the instability of their virial shocks ([Birnboim & Dekel 2003](#); [Dekel & Birnboim 2006](#)). Therefore, any O VI observed around these galaxies must originate from the IGM. The agreement of our basic IGM model with observations in this mass range supports the idea that a simple, photoionized IGM plays a significant role in warm-ion absorption line observations.

In the bottom panel of Figure 3 we display the fraction (percent) of the (halo-averaged) IGM column density from the (halo-averages) total column densities, for $f_{\text{shock}} = 1$. The dashed horizontal line marks a 50% threshold. This figure indicates that on average, the IGM contribution never drops below $\sim 40\%$. Over a significant range of stellar masses, the dominant contribution to the observed O VI column seems to originate in the IGM rather than in the shock-heated halo.

This suggests that physical processes associated with the CGM may play smaller roles than often attributed to them, when it comes to O VI absorption.

We now explore how these results depend on redshift, and whether they are specific to O VI or may apply to additional warm-ion absorption signatures. We thus repeat the analysis for halos with masses in the range $10^{11} - 10^{14} M_{\odot}$, at redshifts in the range $0.9 < z < 0.02$. In Figures 4 and 5, we display results assuming impact parameters, $b = 100$ and 0 kpc, respectively. Since observations at $b = 0$ will realistically be dominated by the central galaxy, we only integrate starting at $0.1R_{\text{vir}}$, which we assume to be the galaxy radius. The columns for $b = 0$ represent the maximum possible CGM contribution. We display results for O VI, N V, and Si IV.

Figure 4 follows the $M_{\text{vir}} - z$ evolution of many halos. Each curve represents the evolution of a single halo and is color-coded by the fraction of IGM contribution to the total column density of O VI (left panel), N V (middle panel), and Si IV (right panel). The fractions are evaluated at an impact parameter $b = 100$ kpc, assuming $f_{\text{shock}} = 1$. The figure shows that the IGM contribution is lowest for masses between $10^{11} - 10^{11.6} M_{\odot}$ and at low redshifts, $z \lesssim 0.1$. Even then, the IGM contributes tens of percent of the total columns.

This trend may be readily explained by ion fraction distributions such as those displayed in Figure 1. At high redshifts (low halo masses) the virial temperature is too low, and the halo gas density is too high, to allow efficient O VI production either via photo-ionization or via collisional ioniza-

³ As before, integrating from $\max(0.1R_{\text{vir}}, b)$ to 3 Mpc for the total column, and from R_{shock} to 3 Mpc for the IGM columns

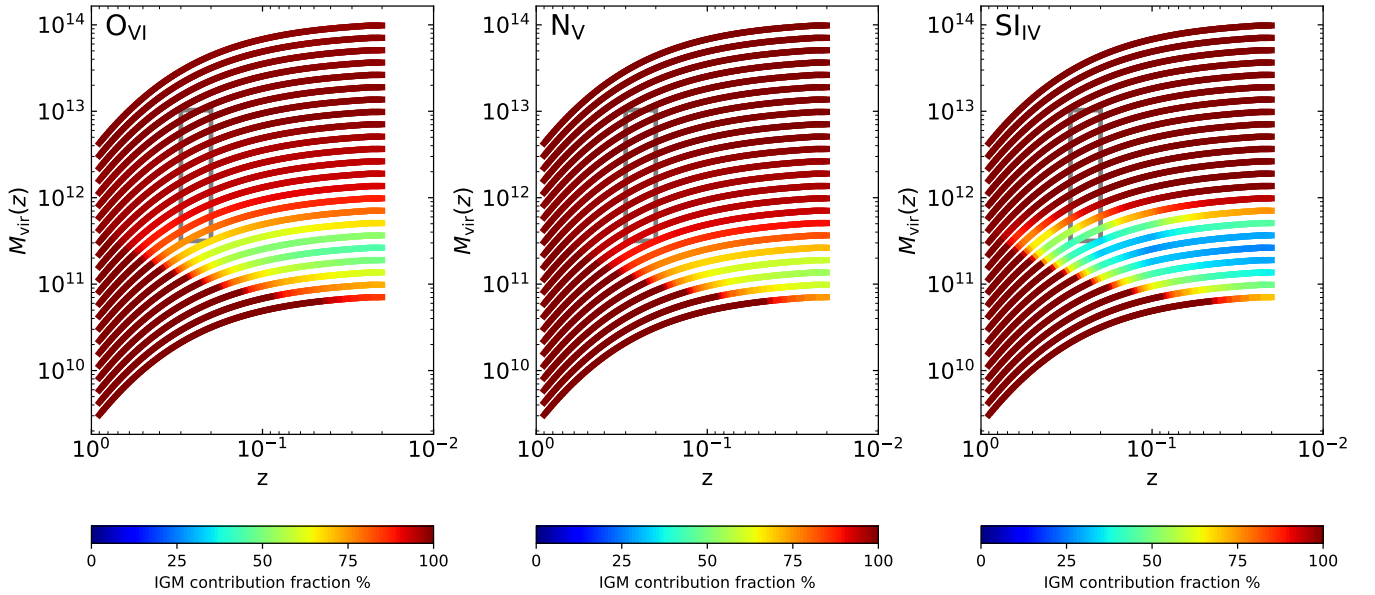


Figure 4. Virial mass vs. redshift curves, color-coded by the fraction of IGM contribution to the total columns at an impact parameter, $b = 100$ kpc, for $f_{\text{shock}} = 1$. Each curve follows a single halo’s trajectory. Left: O VI contribution fractions; middle: N V contribution fractions; right: Si IV contribution fractions. The gray rectangular frame roughly indicates the parameter space probed by *COS-Halos* survey (Werk *et al.* 2016).

tion. Later, intermediate mass halos have a virial temperature and densities ideal for efficiently producing O VI within the CGM, especially in the inner parts of the halo. As the halos further grow and evolve, the virial temperature surpasses the optimal CPIO value for O VI, thus diminishing CGM contribution. The relative CGM contribution therefore has an optimal mass/redshift regime. The same logic follows for N V and Si IV.

In the IGM, however, the ion fraction profiles weakly depend on halo mass or redshift, ensuring a steady contribution to the total observed columns. This is due to the concerted action of two effects: the decline in density with cosmic evolution, and the decreasing intensity of the *UV* background, which (for the redshift and mass range that we consider) result in a constant ionization parameter, to within a factor of 2, in the nearby IGM.

Figure 4 shows that the IGM always significantly contributes to the total column density. For reference, we also mark a rough representation of the $M_{\text{vir}} - z$ region (gray rectangle) probed by *COS-Halos* survey (Werk *et al.* 2013). In all three panels, the observed parameter space resides well within the region where the IGM contribution to the absorption-line columns is expected to be dominant. This gives further indication that interpreting the observed columns as emanating from the CGM exclusively, may be inaccurate.

For completeness, we also show the IGM contribution fractions for lines of sight through the center of the halos (i.e. $b = 0$ kpc) in figure 5. The lower impact parameter naturally maximizes the halo’s contribution to the ion columns.

This is both due to the larger path length through the halo and because the inner parts of the halo produce O VI more efficiently (see Figure 1). The corresponding IGM fractions are therefore lower. However, even in this case, the *COS-Halos* survey parameter space mostly resides in regions where the IGM seems to dominate the observed columns.

3.3. Simulated Absorption-Line Profiles

Our simple 1D models suggest that significant fractions of O VI and other warm-ions observed in CGM surveys may arise in the photoionized IGM surrounding the shocked halos. We therefore explore whether the two components may be kinetically distinct. For this purpose, we compute the line profiles that are expected to arise due to the combined contributions of the virialized hot CGM and the warm, photoionized infalling IGM. As described in Section 2.5, we assume thermal broadening within each shell, as we integrate through the line-of-sight velocity profile for a given impact parameter (see Appx. A). We verify our procedure by comparing to mock observations of *COS* synthesized from our profiles by the TRIDENT numerical package, as well as to observed line profiles from Werk *et al.* (2013).

Figure 6 shows a comparison between our results for the absorption line profile of the total gas (solid blue), and that of the IGM only (dashed orange). It also shows the absorption line produced by the TRIDENT Python package for the same data, for the total gas (solid gray) and the IGM-only (dashed gray). The TRIDENT profiles also include galactic foregrounds and noise to mimic HST-*COS* observations.

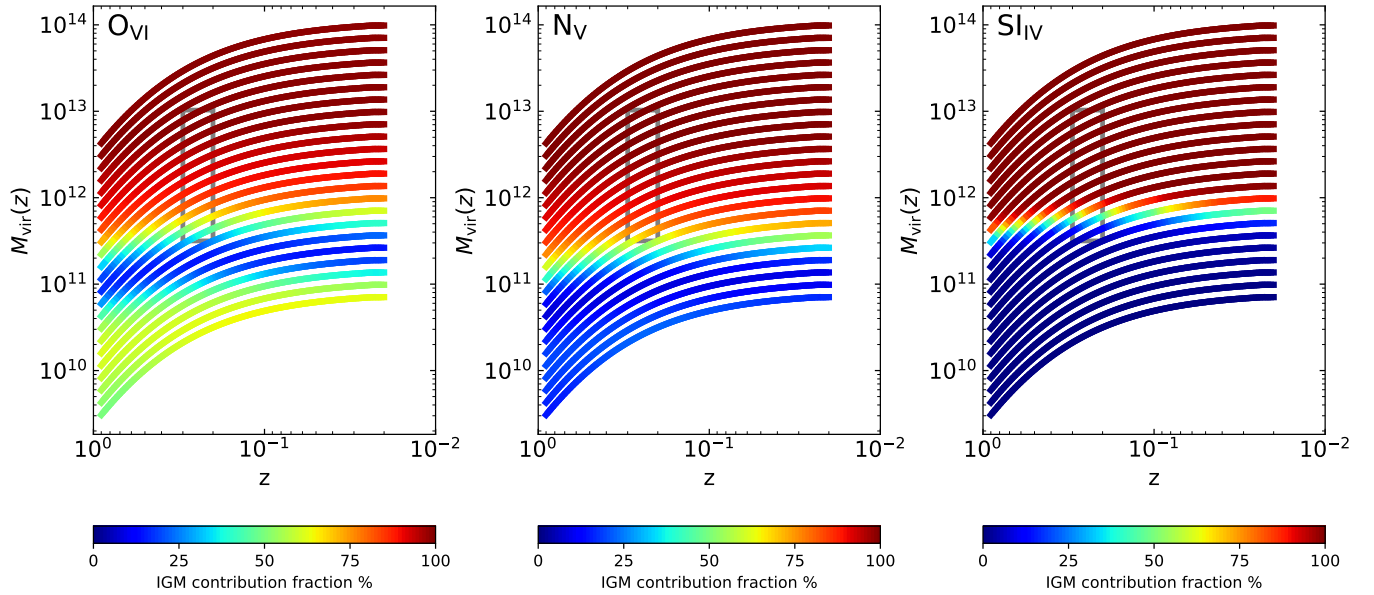


Figure 5. Same as Figure 4, but for an impact parameter $b = 0$ kpc. From left to right, we show the IGM contributions for O VI, N V, and Si IV column densities.

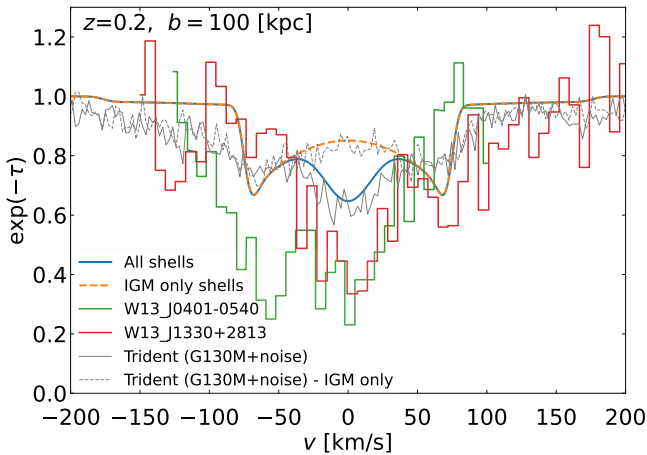


Figure 6. Top: Simulated absorption line profiles for a $10^{12} M_{\odot}$ halo at $z = 0.2$ assuming an impact parameter $b = 100$ kpc. The blue curve is the profile including all gas between $0.1R_{\text{vir}} - 3$ Mpc. The dashed orange curve is for IGM only (namely, $R_{\text{shock}} - 3$ Mpc). The solid gray curve is a synthesized absorption line profile created with the *Trident* Python package, which includes Milky-way foreground, line-spread-function, and Gaussian noise. The dashed gray curve is the *Trident* result for the IGM only.

There is an apparent difference between the total and the IGM-only profiles near the line center, where the hot, virialized, low-velocity CGM gas is present. Aside from the line-center, there are two absorption-‘dips’, one from each side of the center. These are a result of the infalling IGM gas as well as the expanding gas beyond the turnaround radius. The infall velocity is largest at R_{shock} where the gas is closest to the halo. This is also where the IGM density is maximal. The maximal infall velocity is set by the ratio between the

halo mass and its radius ($v_{\text{max}}^2 \approx GM_{\text{vir}}/R_{\text{shock}}$). A well-resolved kinematic structure of an absorption line may thus allow us to discern IGM from CGM contributions, as well as constrain the halo’s physical characteristics. For example, a kinematic structure composed of only two distinct absorption components may indicate that the IGM contribution dominates over the CGM columns.

While the kinematic difference between the total and IGM-only profiles seems sufficient for differentiation in our toy model, this “three-dip” structure will likely often not be distinct in observations of astrophysical halos, due to the complex morphology and kinematics of their multiphased CGM.

To compare our idealized profiles with observational data, we display in figure 6, as examples, data for two absorption line profiles extracted from [Werk et al. \(2013\)](#): For J1330+2813 (red) and J0401-0540 (green). Both lines exhibit stronger overall absorption than our model. The J1330+2813 line shows a dip structure similar to the one in our model, consisting of one central dip (at $v \simeq 0$ km/s), and two additional dips, one on each side of the line-center ($v \simeq -130, 75$ km/s). The J0401-0540 line shows a different structure, with two prominent dips ($v \simeq 0, -50$ km/s). Such structures may hint at additional contributions to the profile, other than the static halo, such as outflows, satellites, asymmetric accretion, etc.

4. CONCLUSIONS & DISCUSSION

In this work, we used a simple $1D$ toy model to compute the cosmological collapse of dark matter halos and their baryonic content around small initial density perturbations. We computed the distributions and densities of the dark matter and gas as functions of time, from redshift $z = 100$ up to the

present day assuming a spherical collapse of the dark matter in an expanding EdS Universe. Using CLOUDY, we obtained the gas PIE temperatures due to the UV background radiation, and the ion fractions of various ions both outside (PIE) and inside (forcing the temperature to T_{vir} when $T_{\text{vir}} > T_{\text{PIE}}$) the evolving halo.

Our results indicate that a significant fraction of the column densities of warm ions (O VI, N V, and Si IV) observed near galaxies may originate from the inner IGM envelopes rather than the shocked CGM. The IGM envelopes are often neglected when interpreting such observations.

We compute the IGM contribution fraction, as a function of the virial mass and redshift. We show that this fraction strongly depends on the halo's virial mass and on the impact parameter. For example, the minimal IGM contribution for O VI columns is obtained for $M \simeq 10^{11} - 10^{11.6} M_{\odot}$. Even then, the IGM contribution remains significant (with a minimum of $\sim 15\%$ for an impact parameter of 0 kpc).

For the mass range probed by most CGM surveys, (which is typically $\gtrsim 10^{11.5} M_{\odot}$), our model indicates that the IGM contribution to the total columns is significant and likely dominant.

The column densities computed with our models are in broad agreement with observational data, both within and outside the halos (see Figure 2), and also closely match the surface averaged values (Figure 3).

Our CGM model is quite basic and therefore fails to capture numerous intricate aspects of astrophysical halos, such as the morphological, thermal, and dynamical details of the multi-phased CGM or the radiative and dynamical properties of accretion shocks. Despite these limitations, it broadly matches the observed column densities both inside and outside the halo, as well as more complex estimates. We note, that the column densities predicted by our model are sensitive to the assumed density and metallicity profiles. However, our main focus in this work has not been on a quantitative estimation of the observed column densities but rather on a qualitative evaluation of the IGM's contribution to the warm-ion absorption. We find our simplified model to be adequate for this specific purpose.

Finally, we composed synthetic absorption line profiles to test whether the CGM and IGM contributions to the total absorption may be discerned kinematically. We demonstrated that a typical line profile is composed of a central (zero-velocity) wide component arising due to the hot CGM, and of two velocity-shifted features that emanate from the infalling IGM envelopes and expanding gas beyond turnaround, forming a "three-dip" structure. These synthetic spectra should, however, be taken with a grain of salt, since real-life halos do not have a perfectly static (0-velocity) CGM, but rather exhibit complex velocity structures: Galactic winds, stellar activity, and turbulence may all contribute to velocities of order hundreds km/s anywhere up to the virial radius. Thus, separating the CGM and IGM contributions in observed profiles will likely prove challenging (see Figure 6). Additional complications may arise due to asymmetric infall of the IGM since filaments, sheets, and satellite halos can also cause asymmetric line profiles, as often observed.

We conclude that the photoionized IGM envelopes of galactic halos may contribute significantly - and possibly dominantly - to the observed warm-ion column densities in CGM surveys. This contribution should be taken into account when attempting to gain insight into the physical processes in the CGM. The inclusion of an IGM contribution may affect the inferred thermal properties and the conclusions regarding the role of non-thermal components and instabilities inside halos.

In a follow-up work, we intend to extend this study to include a more realistic, hydrodynamic spherical collapse model, which better represents the formation and structure of virial shocks. We will also include the influence of the UV background and local ionizing sources, and take departures from ionization equilibrium into account. Our more realistic model may be more directly applicable to interpreting CGM observations.

- 1 This research was supported by the ISRAEL SCIENCE
- 2 FOUNDATION (grant No. 2190/20).

Software: Astropy (Astropy Collaboration et al. 2013, 2018, 2022), CLOUDY (Ferland et al. 2017; Chatzikos et al. 2023), YT analysis toolkit (Turk et al. 2011) Trident (Hummels et al. 2017)

REFERENCES

- Appleby, S., Dave, R., Sorini, D., Cui, W., & Christiansen, J. 2022, arXiv e-prints, arXiv:2207.04068.
<https://arxiv.org/abs/2207.04068>
- Astropy Collaboration, Robitaille, T. P., Tollerud, E. J., et al. 2013, A&A, 558, A33, doi: [10.1051/0004-6361/201322068](https://doi.org/10.1051/0004-6361/201322068)
- Astropy Collaboration, Price-Whelan, A. M., Sipőcz, B. M., et al. 2018, AJ, 156, 123, doi: [10.3847/1538-3881/aabc4f](https://doi.org/10.3847/1538-3881/aabc4f)
- Astropy Collaboration, Price-Whelan, A. M., Lim, P. L., et al. 2022, apj, 935, 167, doi: [10.3847/1538-4357/ac7c74](https://doi.org/10.3847/1538-4357/ac7c74)
- Birnboim, Y., & Dekel, A. 2003, MNRAS, 345, 349, doi: [10.1046/j.1365-8711.2003.06955.x](https://doi.org/10.1046/j.1365-8711.2003.06955.x)

- Chatzikos, M., Bianchi, S., Camilloni, F., et al. 2023, *RMxAA*, 59, 327, doi: [10.22201/ia.01851101p.2023.59.02.12](https://doi.org/10.22201/ia.01851101p.2023.59.02.12)
- Dalton, T., Morris, S. L., Fumagalli, M., & Gattuzi, E. 2021, *Monthly Notices of the Royal Astronomical Society*, 508, 1701–1718, doi: [10.1093/mnras/stab2597](https://doi.org/10.1093/mnras/stab2597)
- . 2022, *Monthly Notices of the Royal Astronomical Society*, 513, 822–834, doi: [10.1093/mnras/stac814](https://doi.org/10.1093/mnras/stac814)
- Dekel, A. 1981, *A&A*, 101, 79
- Dekel, A., & Birnboim, Y. 2006, *MNRAS*, 368, 2, doi: [10.1111/j.1365-2966.2006.10145.x](https://doi.org/10.1111/j.1365-2966.2006.10145.x)
- Draine, B. T. 2011, *Physics of the Interstellar and Intergalactic Medium* (Princeton Univ. Press, Princeton, NJ)
- Faerman, Y., Sternberg, A., & McKee, C. F. 2017, *ApJ*, 835, 52, doi: [10.3847/1538-4357/835/1/52](https://doi.org/10.3847/1538-4357/835/1/52)
- . 2020, *ApJ*, 893, 82, doi: [10.3847/1538-4357/ab7ffc](https://doi.org/10.3847/1538-4357/ab7ffc)
- Ferland, G. J., Chatzikos, M., Guzmán, F., et al. 2017, *The 2017 Release of Cloudy*. <https://arxiv.org/abs/1705.10877>
- Gattuzi, E., Wilms, J., Hämmerich, S., & Arcodia, R. 2024, *A&A*, 683, A213, doi: [10.1051/0004-6361/202348705](https://doi.org/10.1051/0004-6361/202348705)
- Girelli, G., Pozzetti, L., Bolzonella, M., et al. 2020, *A&A*, 634, A135, doi: [10.1051/0004-6361/201936329](https://doi.org/10.1051/0004-6361/201936329)
- Gutcke, T. A., Stinson, G. S., Macciò, A. V., Wang, L., & Dutton, A. A. 2017, *MNRAS*, 464, 2796, doi: [10.1093/mnras/stw2539](https://doi.org/10.1093/mnras/stw2539)
- Haardt, F., & Madau, P. 2012, *ApJ*, 746, 125, doi: [10.1088/0004-637X/746/2/125](https://doi.org/10.1088/0004-637X/746/2/125)
- Ho, S. H., Martin, C. L., & Schaye, J. 2021, *ApJ*, 923, 137, doi: [10.3847/1538-4357/ac2c73](https://doi.org/10.3847/1538-4357/ac2c73)
- Hummels, C. B., Smith, B. D., & Silvia, D. W. 2017, *The Astrophysical Journal*, 847, 59, doi: [10.3847/1538-4357/aa7e2d](https://doi.org/10.3847/1538-4357/aa7e2d)
- Johnson, J. L. 2012, *Formation of the First Galaxies: Theory and Simulations* (Springer Berlin Heidelberg), 177–222, doi: [10.1007/978-3-642-32362-1_4](https://doi.org/10.1007/978-3-642-32362-1_4)
- Johnson, S. D., Chen, H.-W., & Mulchaey, J. S. 2015, *Monthly Notices of the Royal Astronomical Society*, 449, 3263, doi: [10.1093/mnras/stv553](https://doi.org/10.1093/mnras/stv553)
- Lehner, N., O’Meara, J. M., Fox, A. J., et al. 2014, *ApJ*, 788, 119, doi: [10.1088/0004-637X/788/2/119](https://doi.org/10.1088/0004-637X/788/2/119)
- Lehner, N., Wotta, C. B., Howk, J. C., et al. 2019, *The Astrophysical Journal*, 887, 5, doi: [10.3847/1538-4357/ab41fd](https://doi.org/10.3847/1538-4357/ab41fd)
- McQuinn, M., & Werk, J. K. 2018, *The Astrophysical Journal*, 852, 33, doi: [10.3847/1538-4357/aa9d3f](https://doi.org/10.3847/1538-4357/aa9d3f)
- Muzahid, S., Srianand, R., Bergeron, J., & Petitjean, P. 2012, *MNRAS*, 421, 446, doi: [10.1111/j.1365-2966.2011.20324.x](https://doi.org/10.1111/j.1365-2966.2011.20324.x)
- Nelson, D., Kauffmann, G., Pillepich, A., et al. 2018, *Monthly Notices of the Royal Astronomical Society*, 477, 450, doi: [10.1093/mnras/sty656](https://doi.org/10.1093/mnras/sty656)
- Oppenheimer, B. D., Schaye, J., Crain, R. A., Werk, J. K., & Richings, A. J. 2018, *Monthly Notices of the Royal Astronomical Society*, 481, 835, doi: [10.1093/mnras/sty2281](https://doi.org/10.1093/mnras/sty2281)
- Oppenheimer, B. D., Crain, R. A., Schaye, J., et al. 2016, *MNRAS*, 460, 2157, doi: [10.1093/mnras/stw1066](https://doi.org/10.1093/mnras/stw1066)
- Planck Collaboration, Ade, P. A. R., Aghanim, N., et al. 2016, *A&A*, 594, A13, doi: [10.1051/0004-6361/201525830](https://doi.org/10.1051/0004-6361/201525830)
- Prochaska, J. X., Weiner, B., Chen, H. W., Cooksey, K. L., & Mulchaey, J. S. 2011a, *ApJS*, 193, 28, doi: [10.1088/0067-0049/193/2/28](https://doi.org/10.1088/0067-0049/193/2/28)
- Prochaska, J. X., Weiner, B., Chen, H. W., Mulchaey, J., & Cooksey, K. 2011b, *ApJ*, 740, 91, doi: [10.1088/0004-637X/740/2/91](https://doi.org/10.1088/0004-637X/740/2/91)
- Qu, Z., & Bregman, J. N. 2018, *ApJ*, 856, 5, doi: [10.3847/1538-4357/aaaf4d](https://doi.org/10.3847/1538-4357/aaaf4d)
- Ryden, B. 2017, *Introduction to Cosmology* (Cambridge University Press). <https://books.google.co.il/books?id=07WSDQAAQBAJ>
- Shen, S., Madau, P., Aguirre, A., et al. 2012, *ApJ*, 760, 50, doi: [10.1088/0004-637X/760/1/50](https://doi.org/10.1088/0004-637X/760/1/50)
- Shull, J. M., Smith, B. D., & Danforth, C. W. 2012, *The Astrophysical Journal*, 759, 23, doi: [10.1088/0004-637x/759/1/23](https://doi.org/10.1088/0004-637x/759/1/23)
- Stern, J., Faucher-Giguère, C.-A., Hennawi, J. F., et al. 2018, *ApJ*, 865, 91, doi: [10.3847/1538-4357/aac884](https://doi.org/10.3847/1538-4357/aac884)
- Stern, J., Hennawi, J. F., Prochaska, J. X., & Werk, J. K. 2016, *ApJ*, 830, 87, doi: [10.3847/0004-637X/830/2/87](https://doi.org/10.3847/0004-637X/830/2/87)
- Strawn, C., Roca-Fàbrega, S., Primack, J. R., et al. 2024, *The Astrophysical Journal*, 962, 29, doi: [10.3847/1538-4357/ad12cb](https://doi.org/10.3847/1538-4357/ad12cb)
- Suresh, J., Rubin, K. H. R., Kannan, R., et al. 2017, *MNRAS*, 465, 2966, doi: [10.1093/mnras/stw2499](https://doi.org/10.1093/mnras/stw2499)
- Tchernyshyov, K., Werk, J. K., Wilde, M. C., et al. 2022, *ApJ*, 927, 147, doi: [10.3847/1538-4357/ac450c](https://doi.org/10.3847/1538-4357/ac450c)
- Tumlinson, J., Peebles, M. S., & Werk, J. K. 2017, *ARA&A*, 55, 389, doi: [10.1146/annurev-astro-091916-055240](https://doi.org/10.1146/annurev-astro-091916-055240)
- Tumlinson, J., Thom, C., Werk, J. K., et al. 2011, *Science*, 334, 948, doi: [10.1126/science.1209840](https://doi.org/10.1126/science.1209840)
- Turk, M. J., Smith, B. D., Oishi, J. S., et al. 2011, *The Astrophysical Journal Supplement Series*, 192, 9, doi: [10.1088/0067-0049/192/1/9](https://doi.org/10.1088/0067-0049/192/1/9)
- Voit, G. M. 2019, *ApJ*, 880, 139, doi: [10.3847/1538-4357/ab2bfd](https://doi.org/10.3847/1538-4357/ab2bfd)
- Werk, J. K., Prochaska, J. X., Thom, C., et al. 2013, *ApJS*, 204, 17, doi: [10.1088/0067-0049/204/2/17](https://doi.org/10.1088/0067-0049/204/2/17)
- Werk, J. K., Prochaska, J. X., Cantalupo, S., et al. 2016, *The Astrophysical Journal*, 833, 54, doi: [10.3847/1538-4357/833/1/54](https://doi.org/10.3847/1538-4357/833/1/54)
- Wiersma, R. P. C., Schaye, J., & Theuns, T. 2011, *MNRAS*, 415, 353, doi: [10.1111/j.1365-2966.2011.18709.x](https://doi.org/10.1111/j.1365-2966.2011.18709.x)

APPENDIX

A. KINEMATIC O VI ABSORPTION SPECTRUM

In section 3.3, we present synthetic O VI absorption spectra for lines-of-sight passing through our computational box. Given an impact parameter b , the line-of-sight passes through all the shells with radial distances between b and 3 Mpc.

Each shell is characterized by its distance from the halo center r_i , O VI number density $n(\text{OVI})_i$, temperature T_i , and velocity relative to the halo centroid v_i . The projected line-of-sight velocity of a shell is then $v_{i,\parallel} = v_i \sqrt{1 - (b/r_i)^2}$ (note, $b < r_i < 3$ Mpc). When computing the total absorption through the halo, each shell contributes twice – on the near and far sides of the halo – with opposite line-of-sight velocities, i.e., at $\pm v_{i,\parallel}$.

For the temperatures and optical depths characteristic of the CGM and IGM, the individual shell's line profiles are dominated by thermal broadening, and can therefore be well approximated by Gaussian profiles (e.g. eq. 6.38 from [Draine 2011](#), expressed in terms of velocity),

$$\phi_i^\pm(v) \approx \frac{1}{\sqrt{\pi} b_i} \exp\left(-\frac{(v \pm v_{i,\parallel})^2}{b_i^2}\right),$$

which are centered about $\pm v_{i,\parallel}$ for the near and far sides of the halo. Here $b_i = \sqrt{2k_B T_i/m}$ are the Doppler broadening parameters, and $\int \phi_i^\pm(v) dv = 1$. For O VI absorption, we set $m = m_{\text{O}} \simeq 16m_p$. With this line profile, the absorption cross-section is given by (e.g. [Draine 2011](#), eqn. 6.39),

$$\sigma_i^\pm(v) = \frac{\pi e^2}{m_e c} f \lambda_0 \phi_i^\pm(v) = \frac{\sqrt{\pi} e^2}{m_e c} \frac{f \lambda_0}{b_i} e^{-(v \pm v_{i,\parallel})^2/b_i^2},$$

where f is the oscillator strength for the transition. For our O VI line at $\lambda_0 = 1031.91 \text{ \AA}$, the oscillator strength is $f(\text{OVI}) = 0.1376$ (www.atomdb.org).

The optical depth is then,

$$\tau_v = \sum_i [\sigma_i^+(v) + \sigma_i^-(v)] n(\text{OVI})_i ds_i,$$

where ds_i is the path-length through shell i along the line of sight, $ds_i = (r_{i+1} - r_i)/\sqrt{1 - (b/r_i)^2}$.

Finally, the velocity-dependent intensity is given by,

$$I(v) = I_0(v) e^{-\tau_v}.$$

In creating Figure 6, we assumed a flat incoming spectrum $I_0(v)$.